Inorganic Chemistry Communications 184 (2026) 115860

Contents lists available at ScienceDirect

Inorganic Chemistry Communications

journal homepage: www.elsevier.com/locate/inoche

Research Article

Computational and biological evaluation of palladium(II) complexes as VEGFR-2 inhibitors: a molecular docking, dynamics, and cytotoxicity study

Tuncay Karakurt [a,1], Büşra Kaya [b,2], Onur Şahin [c,3], Elif Avcu Altıparmak [d,4], Tülay Bal-Demirci [d,*,5], Bahri Ülküseven [d,6]

[a] Department of Chemical and Process Engineering, Faculty of Engineering-Architecture, Kırsehir Ahi Evran University, 40100 Kırsehir, Turkey
[b] Cancer Cell Biology and Drug Discovery, Institute for Biomedicine and Glycomics, Griffith University, Southport 4215, Queensland, Australia
[c] Department of Occupat Health & Safety, Faculty of Health Sciences, Sinop University, TR-57000 Sinop, Turkey
[d] Department of Chemistry, Engineering Faculty, Inorganic Chemistry Department, İstanbul University-Cerrahpasa, 34320 İstanbul, Turkey

ARTICLE INFO

Keywords:
Methyl thiosemicarbazone
X-ray
Molecular docking
Molecular dynamics
Binding mechanisms

ABSTRACT

In this study, three novel palladium(II) complexes based on *S*-methylthiosemicarbazone ligands derived from 1,3-butanedione and 2,4-pentanedione—functionalized with methyl (—CH_3), trifluoromethyl (—CF_3), and thiophene groups—were synthesized and structurally characterized by spectroscopic methods and single-crystal X-ray diffraction. To evaluate their potential as VEGFR-2 inhibitors, a comprehensive computational investigation was performed. Molecular docking and molecular dynamics (MD) simulations were employed to assess the binding affinities and dynamic stability of the co-ligand (**colig**) and three complexes (**comp1**, **comp2**, and **comp3**) with the VEGFR-2 receptor (PDB ID: 3CJG).

Binding analyses consistently identified **colig** as the most potent binder, exhibiting the most favorable binding free energy (ΔG_{bind} of −106.282 kJ/mol). MD simulations revealed two distinct stability profiles: *colig* and **comp1** formed highly stable and rigid complexes, confirmed by low RMSD and RMSF values. In contrast, **comp2** and **comp3** were found to be significantly more flexible. Per-residue energy decomposition revealed that this stability is achieved through two different mechanisms: superior van der Waals interactions for *colig*, and a powerful electrostatic anchor with ASP1044 for **comp1**.

Additionally, MTT assays on HUVEC cells revealed low cytotoxicity (IC_{50} > 50 μM) for all synthesized complexes. Considering its high dynamic stability, unique electrostatic binding mechanism, and favorable safety profile, **comp1** emerges as the most promising synthesized candidate for further development. These combined findings provide valuable insights for designing next-generation palladium(II)-based VEGFR-2 inhibitors.

1. Introduction

The discovery of anticancer effects of cisplatin gave rise to the search for new anticancer agents among the groups of metal-containing compounds [1]. In this context, palladium, which is in the same group as platinum, is one of the most studied metals and many of its compounds have been the subject of detailed research [2–6]. A wide variety of organic molecules have been tested by binding to palladium(II), especially thiosemicarbazone derivatives have been frequently preferred due to their well-known activity. Studies have shown that complex molecules containing palladium(II) exhibit various biological activities [7–12].

In previous years, most of the studies have aimed at providing cell death and examining the activity mechanisms. Many palladium(II) complexes have also been examined in such studies [11,13–21]. Since the importance of preventing harmful cell formation is understood,

* Corresponding author.
E-mail address: tulaybal@iuc.edu.tr (T. Bal-Demirci).
[1] ORCID: 0000-0001-6944-9883.
[2] ORCID: 0000-0003-2706-172X.
[3] ORCID: 0000-0003-3765-3235.
[4] ORCID: 0000-0002-5491-8445.
[5] ORCID: 0000-0003-4663-2209.
[6] ORCID: 0000-0001-6342-1505.

https://doi.org/10.1016/j.inoche.2025.115860
Received 20 September 2025; Received in revised form 2 November 2025; Accepted 16 November 2025
Available online 23 November 2025

inhibition of enzymes that play a role in cancer formation is now seen as a viable strategy for cancer treatment. In this context, inhibition of the VEGFR2 signaling pathway is one of the promising approaches for treatment. VEGFR-2 type proteins perceive extracellular signals and initiate signaling pathways within the cell [22–28].

3CJG, a Protein Data Bank code related to VEGFR-2 (Vascular Endothelial Growth Factor Receptor 2), represents a structural analysis of VEGFR-2 [29]. VEGFR-2 has become an important target in areas such as cancer treatment. Cancer cells frequently produce VEGF in response to oxygen deficiency, which leads to the formation of new blood vessels at the cancerous site. That is, VEGF (Vascular Endothelial Growth Factor) activates VEGFR-2, initiating angiogenesis (the formation of new blood vessels), which plays a critical role in wound healing, tumor development, and many other biological events. VEGFR-2 is one of the Vascular Endothelial Growth Factor (VEGF) receptors that are receptor tyrosine kinases, and it interacts with VEGF to regulate vascular formation.

Therefore, VEGFR-2 inhibitors are used in cancer treatments that aim to prevent tumor growth by blocking the development of blood vessels. Blocking VEGFR-2 may be a treatment strategy to prevent cancer growth. When VEGFR2 is blocked, new blood vessels do not form around the tumor. This leads to cancer cells not receiving enough oxygen and nutrients, which can trigger cell death, increase cellular stress, and initiate apoptosis (programmed cell death) processes [30].

The structural data of 3CJG is related to the structural details of VEGFR-2. The receptor VEGFR-2 is an important component of the structure in the 3CJG protein database. The structure in 3CJG generally indicates which ligands VEGFR-2 binds to and the structure of these binding sites. For example, molecules that can bind to the active site of VEGFR-2 could be used as potential drugs designed to block angiogenesis in cancer treatment. The molecule should have minimal toxicity in treated individuals. Therefore, VEGFR-2 inhibitors play a very important role in cancer treatment and strategies to block angiogenesis. This structure helps scientists better understand VEGFR-2 and design potential drugs that can bind to this receptor [31].

A number of organic molecules have been synthesized to be tested for VEGFR-2 inhibition. Some of them are the derivatives of pyrimidine [32,33], nicotinamide [34], Naphthamide [35], pyrazoles, 1,3,4-oxadiazoles, 1,3,4-thiadiazoles, and 1,2,4-triazole-3-thione [36]. Moreover, there are reports on some metal complexes. The ruthenium(II) complexes of some Pyrazolylbenzimidazoles with the general formula [RuII (p-cym)(L)-X] + were capable of inhibiting VEGFR-2 phosphorylation [37]. A palladium(II) saccharinate complex of terpyridine inhibited phosphorylation of the signaling regulators downstream of the VEGFR-2 [38]. A paper reported that the mixed-ligand complex of copper(II) with 2-hydroxyl-benzylidene)-amino]-ethanesulfonic and bipyridine can remarkably inhibit proliferation and to inhibit the growth of cervical cancer by down-regulating the expressions of the important proteins downstream of the VEGF/VEGFR-2 signaling pathway [39]. Another study included a theoretical investigation on VEGFR2 inhibition by using manganese(II), nickel(II), copper(II), and zinc(II) complexes of hydrotris(methimazolyl)borate [40].

This study presents the synthesis, structural characterization, and theoretical evaluation of three palladium(II) complexes bearing N_2O_2-chelating thiosemicarbazone ligands (Fig. 1), with a particular focus on their potential to inhibit VEGFR-2. Molecular docking and molecular dynamics (MD) simulations were employed to investigate the binding modes, affinities, and dynamic behaviors of four ligands—*colig*, **comp1**, **comp2**, and **comp3**—in complex with the VEGFR-2 receptor (PDB ID: 3CJG). Comparative energetic and structural analyses were conducted to elucidate the differences in binding mechanisms and to identify the most stable and promising ligand candidates.

2. Experimental section

2.1. Synthesis

2.1.1. Synthesis of starting materials

The compounds of 2,4-pentanedione -*S*-methylthiosemicarbazone (S1) and 1,1,1-trifloro-2,4-pentanedion-*S*-methylthiosemicarbazone (S2) and 2-thenoyltrifluoroacetone-*S*-methylthiosemicarbazone (S3) were prepared according to the earlier reported literature methods [41–44]. The structures of compounds were checked by means of elemental analysis, infrared and ^{1}H NMR spectra and the data were represented in Electronic Supplementary Material.

2.1.2. Synthesis of complexes

comp1: The starting material S1 (0.2 g, 1 mmol) was mixed with 4-methoxy-2-hydroxybenzaldehyde (0.162 g, 1 mmol) in ethanol (10 mL). Freshly prepared $Li_2[PdCl_4]$ (0.280 g, 1 mmol) was added to the mixture, and it was stirred for 2 h at 50 °C. After the addition of triethylamine (0.1 mmol), the precipitate was filtered, washed with ethanol, and dried under vacuum.

The complexes, **comp2** and **comp3**, were synthesized in the same manner as **comp1**, using S2 as the starting material for **comp2,** and S3 as the starting material for **comp3**. Single crystals were obtained by slow evaporation of a DCM/EtOH (1:2, *v*/v) of the Pd(II) complexes at room temperature.

The color, yield (%), m.p. (°C), μ_{eff} (BM), elemental analysis, FT-IR (ATR, cm^{-1}) and ^{1}H NMR (500 MHz, δ ppm) data of the complexes were given in Electronic Supplementary Material.

2.2. MTT assay

The cytotoxic activities of the compounds against human umbilical vein endothelial cells (HUVEC, ATCC), human lung carcinoma (A549, ATCC) and human colorectal carcinoma (HCT-116, ATCC) cells were evaluated using the MTT (3-(4,5-dimethylthiazol-2-yl)-2,5-diphenyl-2H-tetrazolium bromide) assay according to the method described by Mosmann [45]. Cells were cultured in RPMI-1640 medium

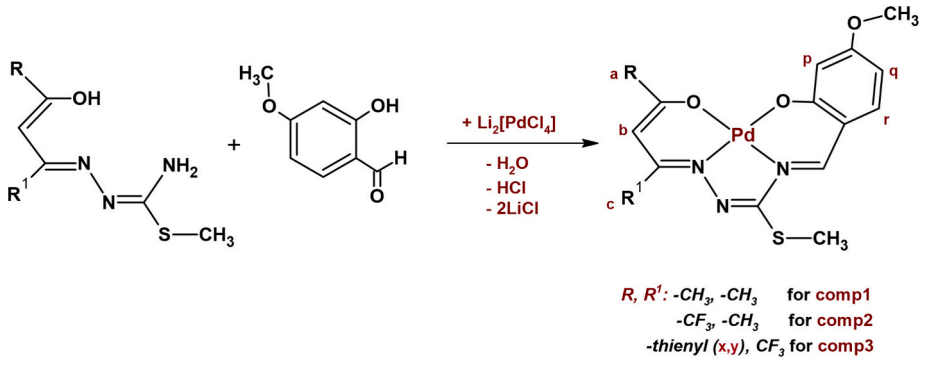

Fig. 1. Schema of the palladium complexes with the proton labelled.

supplemented with 10 % FBS at 37 °C in a humidified atmosphere containing 5 % CO_2. Compounds were initially dissolved in DMSO (5 mg/mL) and further diluted with culture medium to final concentrations of 1, 5, 10, 25, and 50 μM. The final concentration of DMSO in all experiments, including vehicle controls, did not exceed 0.5 % (v/v). Cisplatin (Koçak Farma) was used as a positive control. Cells were seeded into 96-well plates (1×10^4 cells/well for each cell line) and treated with compound solutions for 72 h. Subsequently, MTT solution (0.5 mg/mL in PBS) was added to each well and incubated for 3.5 h. Formazan crystals were dissolved in DMSO, and absorbance was measured at 560 nm with a reference wavelength of 620 nm using a microplate reader.

All experiments were performed in triplicate (three independent replicates for each compound) for all tested cell lines. Cell viability data are expressed as mean ± standard deviation (SD). Statistical analyses were performed using Student's *t*-test to compare treated groups with the control. IC_{50} values were calculated from nonlinear regression using GraphPad Prism 9.

3. Results and discussion

3.1. Synthesis

The palladium complexes, **comp1–3**, were synthesized by reacting 4-methoxysalicylaldehyde with a starting material in equimolar amounts in the presence of Li_2PdCl_4. Starting materials are 2,4-Pentanedione -*S*-methylthiosemicarbazone (S1) and 1,1,1-trifloro-2,4-pentanedion-*S*-methylthiosemicarbazone (S2) and 2-thenoyltrifluoroacetone-*S*-methylthiosemicarbazone (S3). The reaction progress was monitored by thin-layer chromatography (TLC) until the aldehyde was fully consumed. Additionally, complex formation was confirmed by IR spectroscopy based on the disappearance of the free amine and hydroxyl groups characteristic of the thiosemicarbazone starting materials.

The structures of the complexes were characterized by elemental analysis, FT-IR and ^{1}H NMR spectroscopy. Additionally, their structures were elucidated using the X-ray diffraction method (Fig. 2). The data were presented in Electronic Supplementary Material.

3.2. Structural characterization

X-ray: The molecular structures of complexes with the atom numbering schemes are shown in Fig. S1 whilst selected experimental geometric parameters are quoted in Table ST1.

Each Pd(II) ion is coordinated by two oxygen atoms and two nitrogen atoms. Selected bond distances and angles for complexes in Table ST2, the C—H···π, π···π interactions and hydrogen-bond parameters in Table ST3 and the infinite supramolecular network structures in Fig. S2 are given as electronic supplementary information. The Pd—N and Pd—O bond lengths (1.94–2.00 Å) fall within the expected range for similar Pd(II) thiosemicarbazone complexes reported in the literature [46,47], confirming the reliability of the structural model. The Addison distortion index τ for four-coordinate geometry is 0 for square pyramidal (SQP) geometry, 0.85 for triangular-pyramidal (TRP) geometry and 1.00 for tetrahedral (TET) geometry. This τ value is calculated as 0.06 for comp**1–3**. Each Pd(II) ion is coordinated by two nitrogen and two oxygen atoms, resulting in a slightly distorted square-planar geometry.

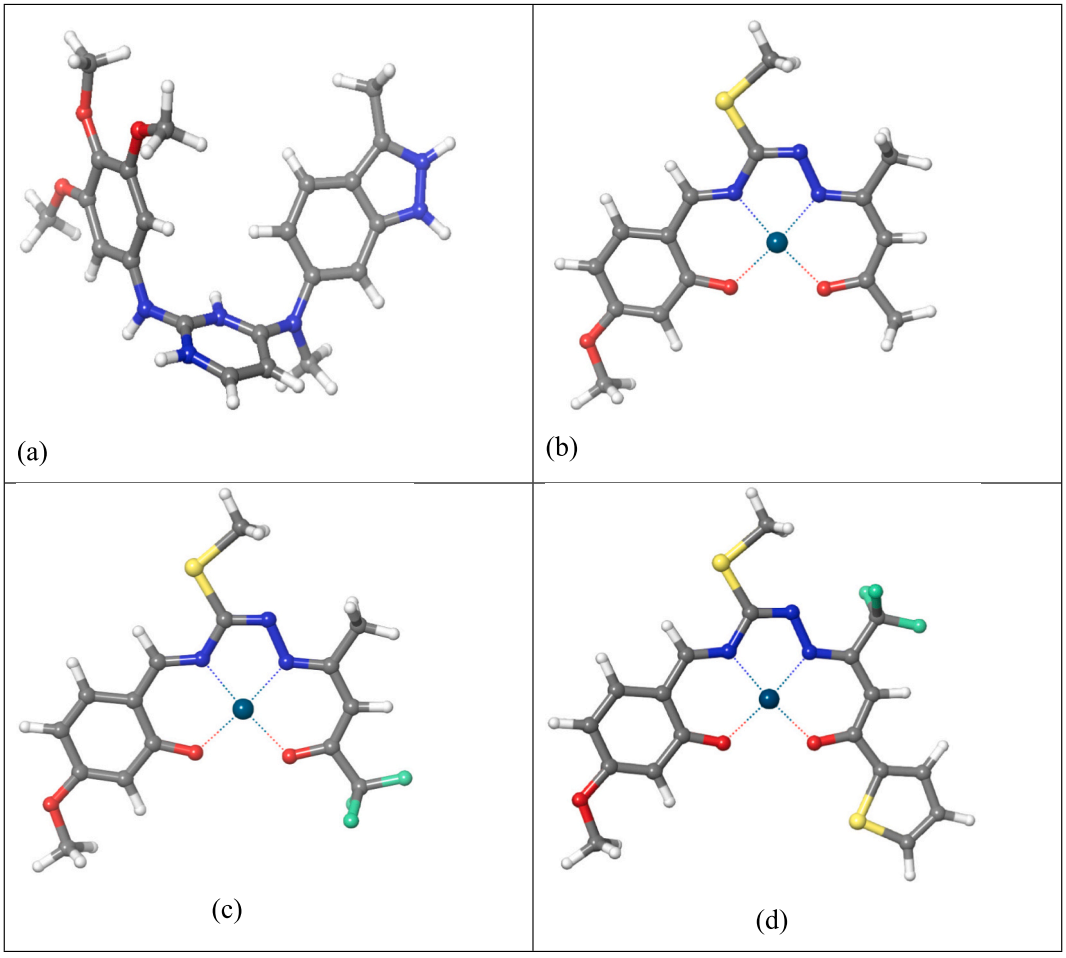

Fig. 2. Optimized structures of (a) *colig* (b) **comp1** (c) **comp2** (d) **comp3.**

While the molecules of **comp1** are connected with C—H···O, C—H···S hydrogen bonds and π···π interactions, the molecules of **comp2** are connected with C—H···O hydrogen bonds, and the molecules of **comp3** are connected with C—H···π interactions (Table S3). In **comp1**, the C2 and C10 atoms acts as hydrogen-bond donors, via atoms H2 and H10B, to atoms S1 in the molecule at (x-1/2, 3/2-y, z-1/2) and O1 in the molecule at (x + 1/2, 3/2-y, z + 1/2), forming $R_2^2(7)$ rings which is running parallel to the [1 0 1] direction (Fig. S2a). **comp1** also contains one π···π interaction which is occurs between the phenyl rings. The distance between the ring centroids is 3.9143(3) Å. In **comp2**, the C10 atom acts as hydrogen-bond donor, via atom H10C, to atom O1 in the molecule at (x + 1, y, z), generate C(7) chain which is running parallel to the [100] direction (Fig. S2b). The molecules of **comp3** are connected by C—H···π interactions (Fig. S2c). The C10 and C18 atoms acts as hydrogen-bond donors to the phenyl rings in the molecule at (1−x, 1/2 + y, 1−z) and (1-x, y-3/2, −z), produce 2D supramolecular network which is running parallel to the *bc* plane.

IR spectroscopy: IR spectra of starting materials and complexes help to understand how the Pd ligand is coordinated and the structural properties of the complex. The transition to the interaction of imine and phenolic groups with Pd leads to significant shifts in the IR spectrum.

When comparing the IR spectra of the complex compounds with those of the starting materials, the absence of amine groups and phenolic OH groups, in the range of 3500–3250 cm^{-1}, in the spectra of the complexes indicates that the second aldehyde has reacted with the amine group, leading to the formation of an additional imine bond. In the IR spectrum of the complexes, **comp1–3**, the **C═N** vibrations are observed at slightly lower frequencies compared to the starting materials, specifically at 1606, 1573, 1560 cm^{-1} for **comp1**, 1617, 1600, 1582 cm^{-1} for **comp2**, and 1614, 1577, 1571 cm^{-1} for **comp3**. This downward shift in frequency compared to the starting materials may be due to the interaction of the C═N bond with the palladium (Pd) center, strengthening the bond or inducing slight structural changes, thereby lowering the vibration frequency [48].

Furthermore, the formation of the complex also proves that the phenolic hydroxyl group in the 4-methoxysalicylaldehyde, which is attached to the starting material, have lost their hydrogen and bound to the palladium in an anionic form.

^{1}H NMR spectroscopy: In the 1H NMR spectrum of the complexes, the peaks belonging to the imine group were recorded as singlets at 8.28 ppm for **comp1**, 9.14 ppm for **comp2** and 7.92 ppm for **comp3**. In **comp2**, the presence of the CF_3 group, a highly electron-withdrawing substituent, causes a substantial deshielding of the imine proton, shifting its signal to a higher chemical shift of 9.14 ppm. This observation reflects the electron-withdrawing effect of the CF_3 group, which decreases the electron density around the imine nitrogen. In **comp3**, the thenoyl and trifluoromethyl groups also exhibit electron-withdrawing effects on the imine proton, but to a lesser extent than in **comp2**. Consequently, the imine proton is observed at 7.92 ppm, suggesting a less pronounced deshielding effect compared to **comp2**. Aromatic protons are clearly observed between 6 and 8 ppm, and the peaks corresponding to S-Methyl groups and methoxy groups are clearly observed between 2.69 and 2.79 ppm and 3.78–3.93 ppm, respectively. The peak corresponding to the b proton in the starting material group was observed at 5.27 ppm for **comp1**, 5.63 ppm for **comp2**, and 6.29 ppm for **comp3**. The b proton was recorded in the deshielded region due to the electron-withdrawing effect of the CF_3 group, which reduces the electron density around it [49].

ESI-MS: The positive ESI-MS of **comp3**, $C_{18}H_{14}F_3N_3O_3PdS_2$, is characterized by a prominent peak at $m/z = 546.8$ Da, corresponding to the monoisotopic mass of the compound. Additionally, a peak at m/z = 547.7 is observed, which corresponds to the protonated molecular ion, $[M + H]^+$. Smaller peaks between $m/z = 545.0$ and m/z = 553.0 were detected, which can be attributed to isotopic variations arising from the natural isotopes of fluorine (F-19 and F-18) and sulfur (S-32 and S-34). A significant peak at $m/z = 569.8$ is also present, likely indicating adduct formation with sodium (Na+), [M + Na]. The most intense peak in the spectrum, m/z = 1117.3, corresponds to a 2 M + Na adduct (100 % relative intensity), indicating the formation of stable fragmentation products. Additional peaks observed between m/z = 1110 and 1126 Da suggest multiple isotopic variants, which further support the structural characterization of the compound. The isotopic distribution of these peaks is consistent with the natural abundances of the constituent elements, providing further confirmation of the molecular structure.

3.3. Molecular docking

This study presents a structure-based molecular docking analysis of the **comp1**, **comp2**, **comp3**, and reference molecule Colig with the VEGFR-2 receptor. The 3CJG structure serves as an important model for understanding how compounds targeting VEGFR-2 bind and provides structural insights into their binding sites. The 3CJG receptor forms a complex structure with the ligand N^4-methyl-N^4-(3-methyl-1H-indazol-6-yl)-N^2-(3,4,5-trimethoxyphenyl)pyrimidine-2,4-diamine (*colig*). This compound belongs to the class of VEGFR-2 tyrosine kinase inhibitors.

Molecular docking simulations were performed to predict the binding affinities and interaction modes of the synthesized compounds with the VEGFR-2 receptor (PDB ID: 3CJG). The results indicated that all compounds successfully docked into the active site of the receptor. Table 1 presents the molecular docking scores, quantitatively indicating the binding affinities of each ligand to the VEGFR-2 receptor.

Among the tested compounds, the *colig* ligand demonstrated the highest binding affinity with a score of −9.07 kcal/mol. This value is significantly lower than those calculated for **comp1** (−6.12 kcal/mol), **comp2** (−6.01 kcal/mol), and **comp3** (−6.05 kcal/mol), suggesting a more stable complex formation with VEGFR-2. The stability of the complex is primarily anchored by a strong conventional hydrogen bond (1.91 Å) formed between the N2 atom of the ligand and the CYS917 residue. This key polar interaction is complemented by an extensive network of hydrophobic interactions, including Pi-Sigma contacts with VAL914 and numerous Alkyl and Pi-Alkyl contacts with residues such as LEU838, LEU1033, VAL846, and PHE916.

The second compound, **comp1**, bound to the VEGFR-2 active site with an affinity of −6.12 kcal/mol. The most notable interaction for this compound is a strong electrostatic attraction (4.96 Å) between its palladium (Pd) atom and the ASP1044 residue. In addition to this ionic attraction, a conventional hydrogen bond with the key residue CYS917 (2.39 Å) and a Pi-Sulfur interaction with PHE1045 contribute to the stability. The binding pose is further secured by a broad network of hydrophobic interactions.

comp2 exhibited a binding affinity of −6.01 kcal/mol, similar to **comp1**. Its binding profile shares common features with **comp1**, including the electrostatic attraction with ASP1044 and a conventional hydrogen bond with CYS917. However, a distinguishing feature for **comp2** is a strong halogen bond formed between its fluorine atom and the LYS866 residue at a short distance of 2.18 Å.

Finally, **comp3** bound to VEGFR-2 with an affinity of −6.05 kcal/mol. The binding mode of this compound is predominantly characterized by halogen bonding. The fluorine atom of **comp3** forms three distinct and strong halogen bonds with the backbone oxygen atoms of LEU838 and GLY839, with distances as short as 2.52 Å and 2.69 Å.

Table 1
Affinity values of *colig* and **comp1, comp2, comp3** molecules as determined by molecular docking.

Receptor	Ligand	Affinity (kcal/mol)
3CJG	*colig*	**−9.07**
	comp1	**−6.12**
	comp2	**−6.01**
	comp3	**−6.05**

The three-dimensional representations in Fig. 3 provide a visual confirmation of the detailed interactions listed in the supplementary information (Tables ST4–ST7). For the ***colig*** ligand, the map in Fig. 3(a) clearly shows the compound deeply embedded within the receptor's hydrophobic pocket (brown surface), aligning with the extensive contacts in Table ST4. Concurrently, Fig. 3(b) highlights the specific hydrogen bond donor/acceptor regions facilitating the key polar interaction with CYS917. For the palladium complexes, the visuals illustrate their settlement within the hydrophobic pocket while distinct colored surfaces correspond to their unique polar interactions. For instance, the

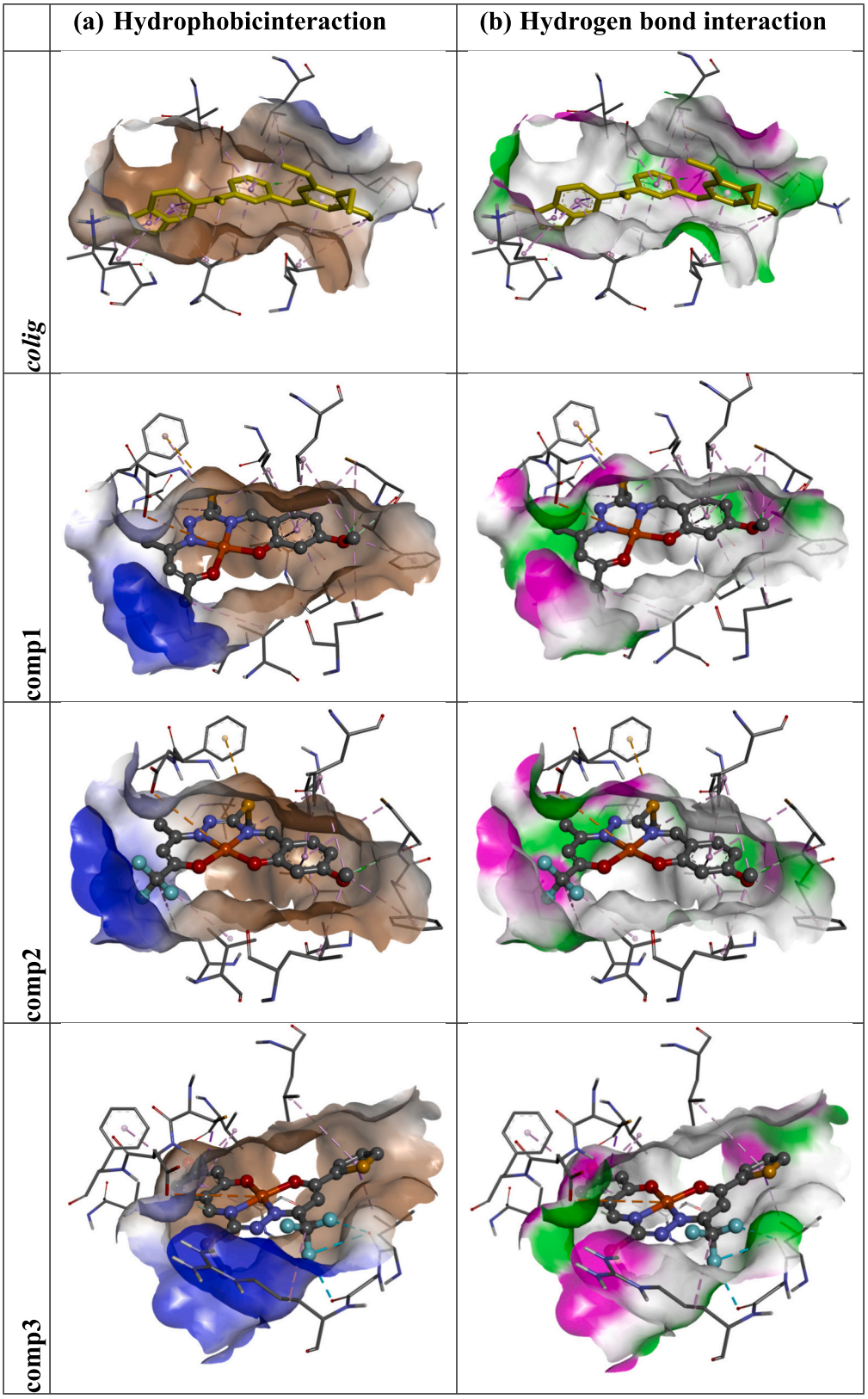

Fig. 3. (a) Hydrophobic interactions and (b) Hydrogen bond interactions for the ligands.

blue surface near **comp1**'s metal center reflects the crucial electrostatic attraction with ASP1044. Although the specific halogen bond for **comp2** is not explicitly visualized by this surface type, its influence is evident in the ligand's stabilized orientation. Lastly, the visualization of **comp3** validates the data in Table ST7, where the dense clustering of hydrogen bond acceptor surfaces (pink) near its fluorine atom visually corresponds to the multiple, critical halogen bonds it forms.

In summary, while the reference ligand *colig* achieves its superior affinity through a powerful hydrogen bond and extensive hydrophobic encapsulation, the synthesized palladium complexes (**comp1**, **comp2**, and **comp3**) exhibit comparable, moderate binding affinities and utilize a different but effective set of interactions, as summarized in Table 2. A common feature for the metal complexes is the electrostatic attraction between the Pd atom and the ASP1044 residue. However, each complex differentiates itself through unique primary interactions (Table 2): **comp1** relies on the combination of this electrostatic pull and a hydrogen bond; **comp2** introduces an additional, strong halogen bond to its binding repertoire; and **comp3**'s stability is almost entirely dictated by a remarkable network of multiple halogen bonds. These findings highlight the diverse molecular strategies through which these compounds, despite their similar predicted inhibitory potential, can effectively occupy the VEGFR-2 active site.

3.4. HOMO-LUMO energy levels and reactivity descriptors

The frontier molecular orbital energies and derived reactivity descriptors are summarized in Table 3. The HOMO (Highest Occupied Molecular Orbital) and LUMO (Lowest Unoccupied Molecular Orbital) energies were extracted from Gaussian output files and converted to electronvolts (1 Hartree = 27.2114 eV). From these values, several important reactivity descriptors were calculated. The HOMO-LUMO energy gap ($\Delta E = E_{LUMO} - E_{HOMO}$) was used to determine the chemical hardness ($\eta = \Delta E/2$) and global softness ($S = 1/2\eta$). Other descriptors, including the chemical potential ($\mu = (E_{LUMO} + E_{HOMO}/2)$, electronegativity ($\chi = -\mu$), and the global electrophilicity index ($\omega = \mu^2/2\eta$), were also calculated.

The HOMO-LUMO energy gap (ΔE) serves as a key indicator of molecular stability and reactivity. Larger energy gaps indicate greater kinetic stability and resistance to electronic excitation, while smaller gaps suggest higher reactivity and polarizability. The spatial distributions of the HOMO and LUMO frontier orbitals for colig, comp1, comp2, and comp3 are depicted in Fig. 4, illustrating the specific regions of each molecule involved in electron-donating and electron-accepting interactions.

Among the studied compounds, the reference ligand *colig* exhibits the largest energy gap (3.796 eV), highest chemical hardness ($\eta = 1.898$ eV), and lowest global softness ($S = 0.263$ eV^{-1}), indicating it is the most electronically stable and least reactive molecule. In contrast, the palladium complexes, particularly **comp3**, display a significantly smaller energy gap ($\Delta E = 2.846$ eV), lower hardness ($\eta = 1.423$ eV) and higher softness ($S = 0.351$ eV^{-1}) suggesting they are intrinsically more reactive and more prone to chemical interactions. Furthermore, the global electrophilicity index (ω) is substantially higher for the palladium complexes (**comp3**: 6.849 eV) compared to *colig* (2.773 eV), suggesting they are much stronger electrophiles.

Table 2
Comparative binding profile summary.

Feature	comp1	comp2	comp3
Docking score (kcal/mol)	−6.12	−6.01	−6.05
Key Polar Interactions	Electrostatic with ASP1044; H-bond with CYS917.	Electrostatic with ASP1044; H-bond with CYS917; Halogen bond with LYS866.	Electrostatic with ASP1044; Multiple Halogen bonds with LEU838 and GLY839.
Hydrophobic Interactions	Extensive Alkyl and Pi-Alkyl contacts.	Extensive Alkyl and Pi-Alkyl contacts.	Extensive Alkyl and Pi-Alkyl contacts.
ATP-Binding Pocket Occupancy	Well-positioned in the active site.	Stabilized orientation via multiple interactions.	Deeply embedded via a network of halogen bonds.
Predicted Inhibitory Potential	Moderate	Moderate	Moderate

Table 3
Quantum chemical parameters and reactivity descriptors.

Parameter	*Colig*	comp1	comp2	comp3	Unit
E_{HOMO}	−5.145	−5.518	−6.123	−5.837	eV
E_{LUMO}	−1.349	−2.397	−2.910	−2.991	eV
Energy Gap (ΔE)	3.796	3.121	3.213	2.846	eV
Chemical Hardness (η)	1.898	1.561	1.607	1.423	eV
Chemical Potential (μ)	−3.247	−3.958	−4.517	−4.414	eV
Electronegativity (χ)	3.247	3.958	4.517	4.414	eV
Electrophilicity Index (ω)	2.773	5.015	6.341	6.849	eV
Global Softness (S)	0.263	0.320	0.311	0.351	eV^{-1}

When these findings are compared with the molecular docking results, an interesting insight emerges. Although *colig* is the least electronically reactive compound according to FMO analysis, it demonstrated the highest binding affinity (−9.07 kcal/mol) in docking simulations. Conversely, the electronically more reactive palladium complexes showed weaker binding scores. This apparent discrepancy highlights that the superior binding affinity of *colig* is predominantly driven by its optimal steric fit and its ability to form strong, specific non-covalent interactions. These interactions, including the key hydrogen bond with CYS917 and extensive hydrophobic contacts, firmly anchor the ligand within the VEGFR-2 active site. The higher electronic reactivity and electrophilicity of the palladium complexes, while significant, do not translate to a higher docking score in this case, indicating that their overall shape and non-covalent interaction profile are less complementary to the binding pocket compared to *colig*.

A more nuanced analysis reveals a direct correlation between the specific electronic property of HOMO energy (E_{HOMO}) and the observed binding affinity. The HOMO energy reflects a molecule's capacity to donate electrons. A clear positive correlation is observed, where *colig*, possessing the highest E_{HOMO} (−5.145 eV) and being the most potent electron donor, also exhibits the strongest binding affinity. The HOMO energy reflects a molecule's capacity to donate electrons. A clear positive correlation is observed, where *colig*, possessing the highest E_{HOMO} (−5.145 eV) and being the most potent electron donor, also exhibits the strongest binding affinity. Conversely, **comp2**, with the lowest E_{HOMO} (−6.123 eV), is the weakest electron donor and correspondingly shows the weakest binding affinity. This suggests that the key non-covalent interactions governing binding within the VEGFR-2 pocket have a significant charge-transfer character. The high electron-donating capacity of *colig* likely strengthens its crucial hydrogen bond with CYS917 and other interactions by allowing for more effective electron density donation to electron-accepting groups in the active site.

In conclusion, achieving high-affinity binding to the VEGFR-2 receptor appears to be a two-part phenomenon. A ligand must first possess the correct shape to fit optimally within the binding pocket. However, to maximize this interaction, it must also have a favorable electronic character. Specifically, a high electron-donating potential, indicated by a high E_{HOMO}, enhances the strength of these sterically-favored non-covalent interactions. *colig* succeeds on both fronts, whereas the synthesized palladium complexes appear to lack the optimal combination of steric fit and specific electron-donating capacity required for superior binding.

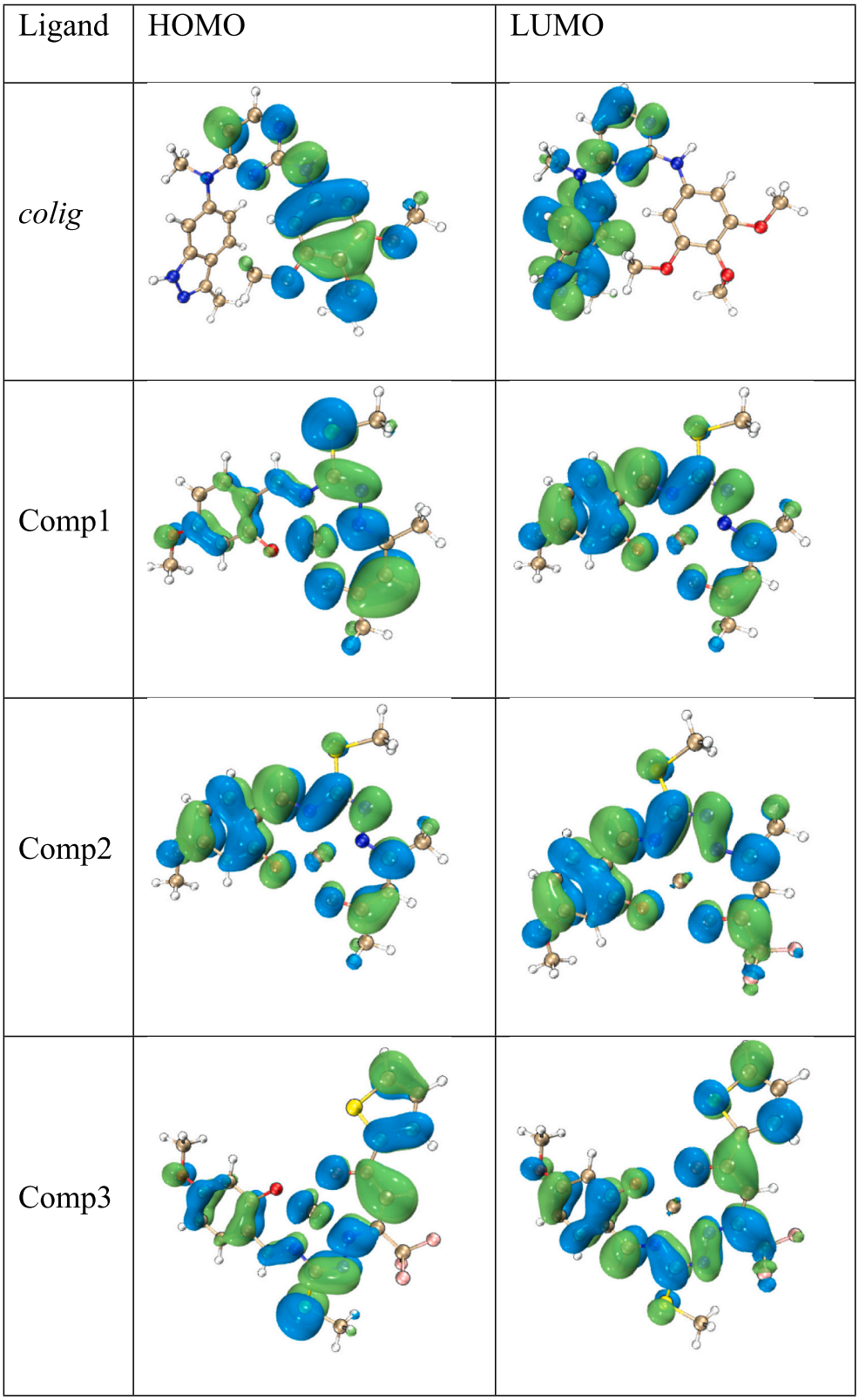

Fig. 4. The spatial distribution of the Highest Occupied (HOMO) and Lowest Unoccupied (LUMO) molecular orbitals for the studied ligands.

3.5. Molecular dynamic

Molecular dynamics (MD) simulations were conducted using the GROMACS 2024 [50] software. The simulation systems were prepared in the Amber package and adapted for compatibility with GROMACS. The initial structures of the systems were generated using AmberTools [51]. The simulation was carried out in three stages. First, energy minimization was performed using the steepest descent algorithm for 50,000 steps. Next, an NVT simulation was conducted for 100 ps at 300 K to equilibrate the system temperature, employing the V-rescale

thermostat. Subsequently, an NPT simulation was performed for 100 ps at 1 atm pressure using the Parrinello-Rahman barostat for pressure equilibration. The production simulation was conducted for a total of 10.000 ps (10 ns) with a time step of 2 fs, and coordinate data were recorded every 10 ps. Periodic boundary conditions were applied throughout the simulation, and center-of-mass (COM) motion removal was enforced to ensure stable modeling of all system components. To neutralize the systems, Cl^- ions were added to the *colig*-receptor, **comp1**-receptor, and **comp2**-receptor systems, whereas Na^+ ions were used for the **comp3**-receptor system (Fig. 5).

The stability of receptor-ligand interactions is assessed using Root Mean Square Deviation (RMSD) analysis in molecular dynamics (MD) simulations. In this study, the binding stabilities of **comp1**, **comp2**, **comp3**, and *colig* with the 3CJG receptor were evaluated based on RMSD values. The analysis utilized time series data, rate of change, moving averages, and distribution graphs. MD simulations serve as a crucial tool for understanding ligand-receptor and ligand-ligand interactions.

To evaluate the structural stability of the protein-ligand complexes, the Root Mean Square Deviation (RMSD) of the protein backbone was calculated over the 10 ns simulation trajectory ((Fig. S3). The RMSD plot reveals distinct stability profiles for the different complexes, which correlate intriguingly with the previously calculated molecular docking affinities.

The *colig*-receptor and **comp1**-receptor systems demonstrate remarkable stability. After an initial equilibration period of approximately 2000–3000 ps, both systems reach a stable plateau, with their RMSD values fluctuating consistently around a low average of approximately **0.25–0.3 nm**. These minimal fluctuations confirm that the protein maintains its native fold and structural integrity when bound to these ligands, indicating the formation of a rigid and stable complex.

In contrast, the **comp2**-receptor and **comp3**-receptor systems exhibit significantly higher flexibility. Their RMSD values are consistently higher, fluctuating in a broader range, mostly between 0.4 nm and 0.6 nm, throughout the simulation. This suggests that the binding of **comp2** and **comp3** induces more pronounced conformational changes or greater dynamic motion in the protein backbone. However, the absence of a continuous upward trend in their RMSD indicates that these systems have reached a different, more flexible, but nonetheless equilibrated state, rather than undergoing denaturation.

When these stability profiles are correlated with the molecular docking results, a compelling narrative emerges. The *colig* ligand, which had the highest binding affinity (−9.07 kcal/mol), also forms one of the most structurally stable complexes, as shown by its low and steady RMSD. This provides a dynamic validation of the docking result,

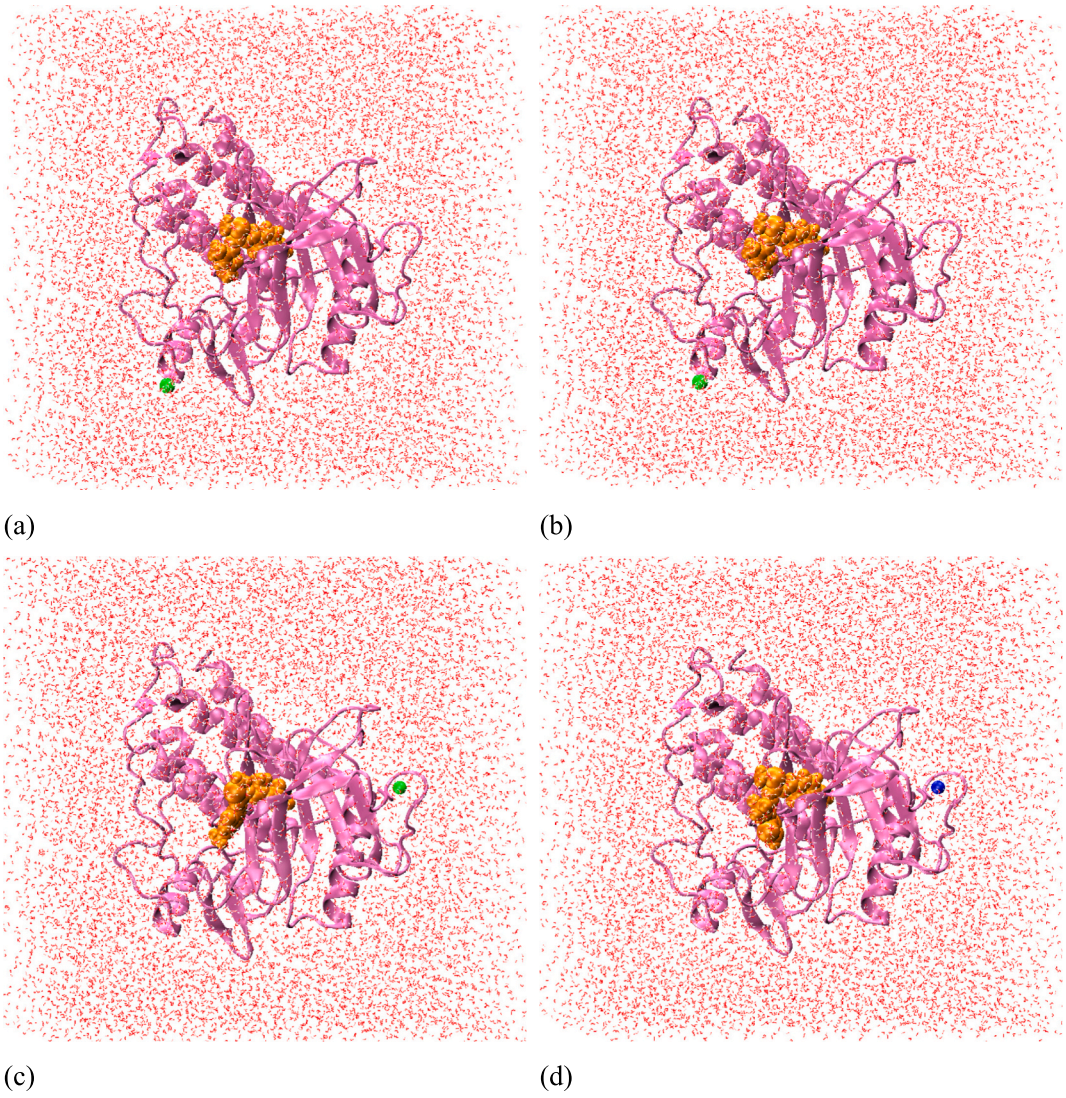

Fig. 5. System filled with water, neutralized with (a) *colig*-receptor, (b) **comp1**-receptor (c) **comp2**-receptor (d) **comp3**-receptor. The ligands, the Na ion, and the Cl ion are all shown in the colors orange, blue, and green, respectively. (For interpretation of the references to color in this figure legend, the reader is referred to the web version of this article.)

suggesting that its strong and specific interactions (particularly the hydrogen bond with CYS917 and extensive hydrophobic fit) effectively "lock" the protein into a rigid, favorable conformation. Interestingly, **comp1**, despite having a significantly weaker binding affinity (−6.12 kcal/mol) than *colig*, induces a similarly high level of structural stability. This implies that its binding mode, anchored by the electrostatic attraction to ASP1044, is also very effective at stabilizing the overall protein structure, even if the total interaction energy is less favorable than that of *colig*. Conversely, the weaker binding affinities of **comp2** (−6.01 kcal/mol) and **comp3** (−6.05 kcal/mol) are mirrored by their higher RMSD values. This suggests that their interaction profiles, which rely more on halogen bonds and less dominant electrostatic forces, may not provide the same rigid structural anchor, thus permitting greater flexibility in the protein backbone.

To further quantify the conformational space sampled by the protein backbone and to assess the flexibility of each complex, RMSD distribution histograms were generated from the 10 ns simulation trajectories (Fig. 6). These histograms illustrate the probability density of the protein backbone residing at a particular RMSD value, providing a clear picture of each system's conformational stability. The analysis reveals two distinct patterns. The *colig*-receptor and **comp1-receptor** systems both exhibit sharp, narrow, and unimodal (single-peaked) distributions centered at approximately **0.28 nm**. This indicates that the protein backbone predominantly occupies a single, stable conformational state throughout the simulation. The narrowness of these peaks signifies low flexibility and confirms that the protein is structurally rigid and well-stabilized when bound to either *colig* or **comp1**. In stark contrast, the **comp2-receptor** and **comp3-receptor** complexes show significantly broader distributions that are shifted toward higher RMSD values, with their peaks centered around 0.4–0.5 nm. This broad distribution indicates that the protein backbone is much more flexible and explores a wider range of conformational states when these ligands are bound. The shift of the peaks to higher RMSD values suggests a deviation from the initial structure to a new, more dynamic equilibrium. These distribution profiles are in excellent agreement with the previous RMSD-over-time analysis and the molecular docking results. The high stability and low flexibility observed for *colig* and **comp1** dynamically validate their effective binding modes, which seem to "lock" the receptor in a specific, rigid conformation. Conversely, the greater flexibility induced by **comp2** and **comp3** is consistent with their slightly weaker and less structurally anchoring interactions, allowing the protein greater conformational freedom.

To further investigate the dynamic stability and the rate of conformational changes of the protein backbone, the RMSD variation rate (dRMSD/dt) was calculated for each complex over the 10 ns simulation (Fig. S4). This parameter measures how rapidly the protein's structure changes at any given moment, with smaller and less frequent fluctuations indicating a more stable and less dynamic system.

The dRMSD/dt plot clearly reinforces the findings from the previous RMSD analyses. The *colig*-receptor and **comp1**-receptor systems exhibit the lowest variation rates. Their dRMSD/dt values remain consistently close to zero, with only minor, low-amplitude fluctuations. This demonstrates that the protein backbone, when bound to these ligands, is not undergoing significant or rapid conformational transitions. This low rate of change is characteristic of a highly stable and structurally converged system, where the complex has settled into a deep energy minimum.

Conversely, the **comp2**-receptor and **comp3**-receptor systems show dRMSD/dt values with significantly larger amplitudes and higher frequencies of fluctuation. These large spikes indicate moments of rapid structural rearrangement within the protein backbone. This behavior is consistent with the higher overall RMSD values observed for these systems and confirms their more dynamic and flexible nature. The protein structure is continuously exploring a broader conformational landscape rather than remaining in a single, stable state.

In conclusion, the analysis of RMSD variation rates provides a more detailed view of the systems' dynamic behavior. The minimal dRMSD/dt fluctuations for *colig* and **comp1** confirm their ability to lock the receptor into a single, stable conformation, consistent with their effective binding modes. The more volatile dRMSD/dt profiles for **comp2** and **comp3** highlight their tendency to induce greater flexibility and conformational dynamism in the receptor, which aligns with their comparatively weaker and less structurally anchoring interactions.

To clearly visualize the equilibration and stability trends of the protein-ligand complexes, the Root Mean Square Deviation (RMSD) of the protein backbone was smoothed using a moving average filter and plotted over the 10 ns simulation time (Fig. 7). This analysis effectively removes high-frequency noise and reveals the underlying conformational behavior of each system. The plot distinctly categorizes the complexes into two groups based on their stability. The *colig*-receptor and **comp1-receptor** systems exhibit high structural stability. After an initial equilibration phase lasting approximately 2000–3000 ps, both systems achieve a stable plateau, with their average RMSD values remaining consistently low, fluctuating around **~0.25–0.3 nm**. This smooth and flat trajectory post-equilibration is a strong indicator that these ligands induce a rigid and stable conformation in the protein, locking it into a well-defined structural state.

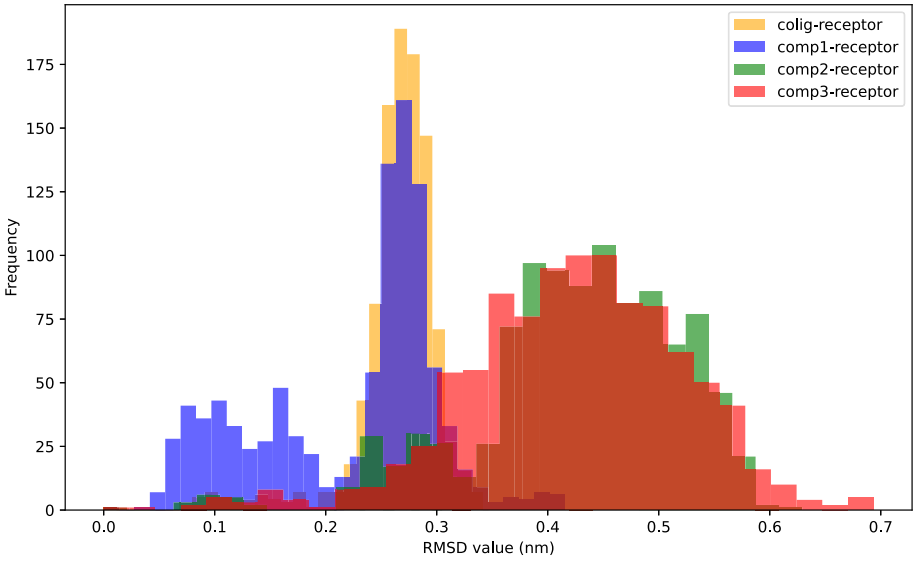

Fig. 6. RMSD distribution plot of four systems (receptor-ligand).

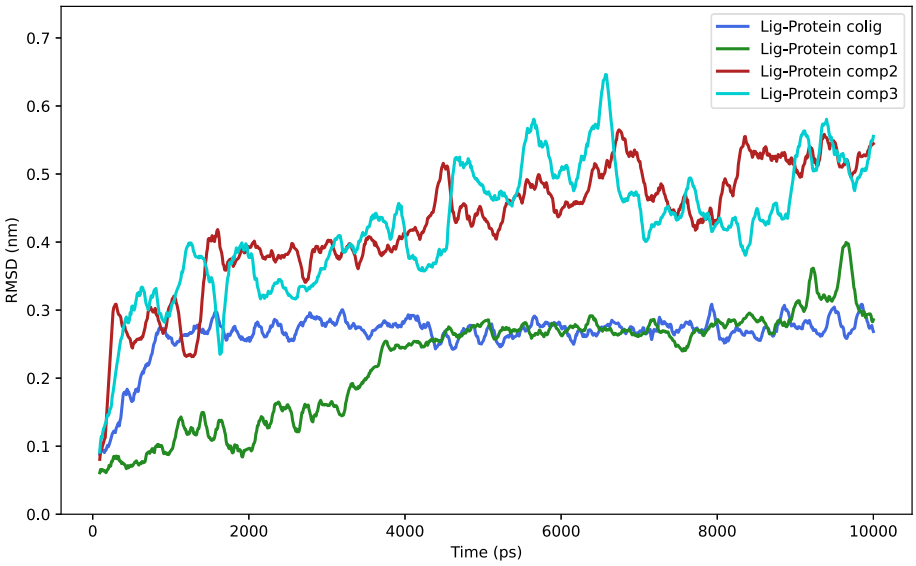

Fig. 7. Moving average graph of RMSD change of four systems.

In contrast, the **comp2-receptor** and **comp3-receptor** systems are characterized by higher structural flexibility. The smoothed RMSD trajectories for these complexes are positioned at a higher range, fluctuating around an average of ~0.4–0.6 nm. While they also reach an equilibrated state (indicated by the lack of a continuous upward trend), the higher average RMSD and the broader, more pronounced undulations in their plots signify greater conformational dynamism. This suggests that the interactions formed by **comp2** and **comp3**, while sufficient to bind to the receptor, allow the protein backbone to explore a wider range of motion and adopt a more flexible, less constrained conformation.

These findings are in excellent agreement with all previous analyses. The superior structural rigidity imparted by *colig* and **comp1** provides a dynamic basis for their effective binding modes observed in docking. Conversely, the increased flexibility associated with **comp2** and **comp3** aligns with their different interaction profiles that permit greater conformational freedom in the receptor.

The RMSD stability profiles detailed previously become more meaningful when explained by the consistency of the ligand-receptor hydrogen bond interactions.

Colig, which stands out as the most stable structure in the RMSD analysis, also consistently maintains 2–5 hydrogen bonds throughout the simulation ((Fig. S5). This persistent hydrogen bond network acts as a strong anchor, locking the receptor into a rigid conformation and thus validating the low RMSD values.

Interestingly, **comp1** also demonstrates high structural stability with a low RMSD, yet it achieves this with an inconsistent and low number of hydrogen bonds. This suggests that the primary source of its stability is not hydrogen bonding, but rather the strong electrostatic attraction with ASP1044 identified in the docking analysis, which appears to be similarly effective at rigidifying the protein.

The more flexible nature (higher RMSD) of **comp2** and **comp3** is also consistent with their interaction profiles. Although **comp2** forms more hydrogen bonds than **comp1**, these interactions, along with its halogen bond, do not provide a sufficient anchor to prevent larger movements in the protein. The highest instability and RMSD values belong to **comp3**, which is explained by its failure to form almost any persistent hydrogen bonds.

In conclusion, it is evident that high stability (low RMSD) requires either a consistent hydrogen bond network (*colig*) or a strong electrostatic anchor **(comp1)**. The absence of such dominant anchors leads to more flexible complexes.

To provide a deeper understanding of the dynamic behavior of the complexes, the Root Mean Square Fluctuation (RMSF) (Fig. S6) of individual protein residues and the non-bonded interaction energies (Lennard-Jones [LJ-SR] and Coulomb [Coul-SR]) (Fig. S7) between each ligand and the receptor were analyzed.

The RMSF analysis, which measures the flexibility of individual amino acid residues, perfectly corroborates the overall stability trends established by the RMSD analysis. The *colig*-receptor and **comp1-receptor** complexes induce the lowest RMSF fluctuations in the protein's binding site residues. This indicates that these ligands effectively reduce the local mobility of the active site, confirming the formation of rigid, stable complexes. In contrast, the binding of **comp2** and **comp3** results in significantly higher RMSF values throughout the receptor, particularly in the binding region. This demonstrates that these ligands cause greater local flexibility and mobility, consistent with the more dynamic nature observed in their RMSD profiles.

The interaction energy calculations provide a clear energetic basis for these observed differences in stability. The exceptional stability (low RMSD and RMSF) of the **comp1-receptor** complex is unequivocally explained by its interaction energy profile: it exhibits by far the strongest and most favorable electrostatic (Coulomb) interaction energy of all the complexes. This confirms that its stability is anchored by a powerful and persistent electrostatic attraction, primarily between the palladium atom and the ASP1044 residue.

Similarly, the high stability of the *colig*-receptor complex is rationalized by it having the strongest (most negative) Lennard-Jones (van der Waals) interaction energy. This finding provides strong evidence that its superior binding is driven by an optimal steric fit and extensive, favorable hydrophobic contacts that maximize stabilizing van der Waals forces.

The less stable complexes, **comp2** and **comp3**, lack such a single, dominant anchoring force. While **comp3** forms strong van der Waals interactions, and **comp2** exhibits a balance of moderate interactions, neither possesses the uniquely powerful electrostatic anchor of **comp1** or the superior van der Waals fit of *colig*. This absence of a dominant stabilizing force results in weaker overall binding and allows for the greater conformational flexibility observed in both their RMSD and RMSF profiles.

3.6. *Binding free energy calculations*

Binding free energy (ΔG_{bind}), a reliable indicator of receptor-ligand interactions, is considered a key parameter for assessing the strength of interactions in biomolecular systems. This value is used to determine

the thermodynamic favorability of a ligand's binding process to its target receptor. A more negative ΔG_{bind} value indicates that the ligand binds more strongly to the receptor, forming a more stable complex, whereas more positive or near-zero values suggest weaker or unstable binding [52]. Binding free energy calculations play a critical role in drug discovery, biotechnology, and biomolecular design. Predicting a ligand's binding potential to a specific target is a crucial step in evaluating the efficacy of drug candidates [53]. Molecular modeling and simulation studies facilitate the computation of binding energy, helping to understand how a given compound interacts with biological targets. One of the most commonly used approaches for these calculations is the Molecular Mechanics/Poisson-Boltzmann Surface Area (MM/PBSA) method. This method estimates binding free energy by considering molecular mechanics (MM) potential energy, solvent effects, and entropic contributions. Compared to experimental techniques, MM/PBSA has lower computational costs, enabling rapid and reliable binding energy calculations for large molecular systems [54]. In receptor-ligand complexes, binding free energy is derived from the combination of molecular mechanics energy, polar and nonpolar solvation energies, and entropic contributions. Molecular mechanics energy encompasses electrostatic and van der Waals interactions, while polar and nonpolar solvation energies represent solvent effects. Entropic factors, on the other hand, describe changes in system disorder during the binding process. The sum of these components determines the overall favorability of ligand binding to the receptor, providing a deeper understanding of biomolecular interactions [55]. In conclusion, binding free energy calculations not only enhance our molecular-level understanding of biological processes but also serve as a powerful guide for drug design, receptor engineering, and biotechnological applications [56].

$$\Delta G_{bind} = \Delta E_{MM} + \Delta G_{polar} + \Delta G_{nonpolar} - T\Delta S \quad (1)$$

Here, binding free energy (ΔG_{bind}) is a crucial parameter for evaluating the strength of receptor-ligand interactions. A more negative ΔG_{bind} value indicates a stronger binding affinity of the ligand to its target receptor. This value is obtained as the sum of various energy components, providing a detailed analysis of molecular interactions.

Molecular mechanics energy (ΔE_{MM}) is a component that includes electrostatic and van der Waals interactions between the receptor and ligand. This energy term contributes to binding strength by assessing direct physical interactions between molecules. Polar solvation free energy (ΔG_{polar}) accounts for the effects of solvent molecules during the binding process. This energy component, calculated using Poisson-Boltzmann or Generalized Born methods, reflects electrostatic interactions mediated by the solvent. Nonpolar solvation free energy ($\Delta G_{nonpolar}$) represents hydrophobic interactions and the contribution of the solvent's nonpolar components to the binding process. Typically estimated using a surface area-dependent model, this component is particularly important for binding events occurring in hydrophobic regions.

To provide a quantitative estimate of the binding affinity, the binding free energies (ΔGbind) for each complex were calculated using the Molecular Mechanics/Poisson-Boltzmann Surface Area (MM/PBSA) method over the 10 ns MD trajectory. The results, summarized in Table 4, not only provide a final ranking of the ligands but also offer a deep energetic rationale for the stability trends previously observed in the RMSD and RMSF analyses.

The calculated binding free energies confirm that *colig* is the most potent binder, with a highly favorable ΔGbind of −106.282 kJ/mol. This aligns perfectly with its top docking score and its exceptional structural stability (low RMSD/RMSF) observed during the simulation. The energy decomposition reveals that this superior affinity is driven by the strongest van der Waals energy (−163.535 kJ/mol), confirming that its stability originates from an optimal steric fit and extensive hydrophobic contacts.

The second most potent ligand is **comp1**, with a strong ΔGbind of −74.742 kJ/mol. This result is perfectly consistent with its high structural stability (low RMSD/RMSF). The energy components reveal a fascinating story: **comp1** possesses by far the strongest electrostatic energy (−105.795 kJ/mol), validating our hypothesis that its stability is derived from a powerful electrostatic anchor. However, it is penalized by a very high (unfavorable) polar solvation energy (194.598 kJ/mol), which prevents it from outperforming *colig*.

The least stable ligands, **comp2** and **comp3**, also have the least favorable binding free energies, at −50.897 kJ/mol and − 58.741 kJ/mol, respectively. This ranking is in excellent agreement with their higher RMSD and RMSF values, confirming their more flexible and less stable nature. Neither of these compounds possesses the dominant van der Waals interactions of *colig* or the powerful electrostatic anchor of **comp1**, leading to weaker overall binding.

In conclusion, the MM/PBSA calculations provide a final and consistent validation of our entire computational analysis. The stability ranking derived from binding free energies (*colig* > **comp1** > **comp3** > **comp2**) perfectly mirrors the structural stability observed in the MD simulations. The data clearly shows that the two most stable ligands achieve their stability through distinct mechanisms: *colig* utilizes superior van der Waals forces driven by its optimal shape complementarity, while **comp1** relies on a dominant electrostatic anchor.

To pinpoint the key amino acid residues driving ligand binding, the total binding free energy (ΔG_{bind}) was decomposed on a per-residue basis (Fig. 8). This analysis provides a definitive, atomic-level explanation for the stability trends and binding mechanisms previously identified.

The decomposition results offer conclusive proof for our binding hypotheses. For *colig*, the analysis confirms that its superior binding affinity is not driven by charged residues. Instead, the most significant favorable contributions come from a series of hydrophobic and aromatic residues, with LEU838, VAL846, LEU887, ALA864, and PHE916 ranking as the top contributors. This finding perfectly aligns with the strong van der Waals energy observed in the MM/PBSA calculation, confirming that *colig*'s stability originates from an optimal shape complementarity that maximizes hydrophobic encapsulation.

The analysis for **comp1** reveals a completely different but equally effective mechanism. The single most dominant contribution to its binding free energy comes from residue ASP1044, with a staggering contribution of −44.5 kJ/mol. This provides the final, unequivocal evidence for our "electrostatic anchor" hypothesis. It demonstrates that the powerful electrostatic attraction between the positively charged palladium center and the negatively charged ASP1044 is the primary force responsible for **comp1**'s high structural stability (low RMSD).

Conversely, the per-residue energy profiles for the less stable ligands, **comp2** and **comp3**, lack a single, overwhelmingly dominant interaction. For **comp2**, the contributions are more modestly distributed

Table 4
Summary Energy (kJ/mol) of receptor-Ligand complex.

System	Van der Waals energy	Electrostatic energy	Polar solvation energy	SASA energy	Binding free energy
colig-receptor	−188.787	−50.511	152.673	−19.657	−106.282
comp1-receptor	−153.381	−99.558	194.598	−16.401	−74.742
comp2-receptor	−143.483	−44.179	154.106	−17.341	−50.897
comp3-receptor	−150.611	−27.769	137.055	−17.417	−58.741

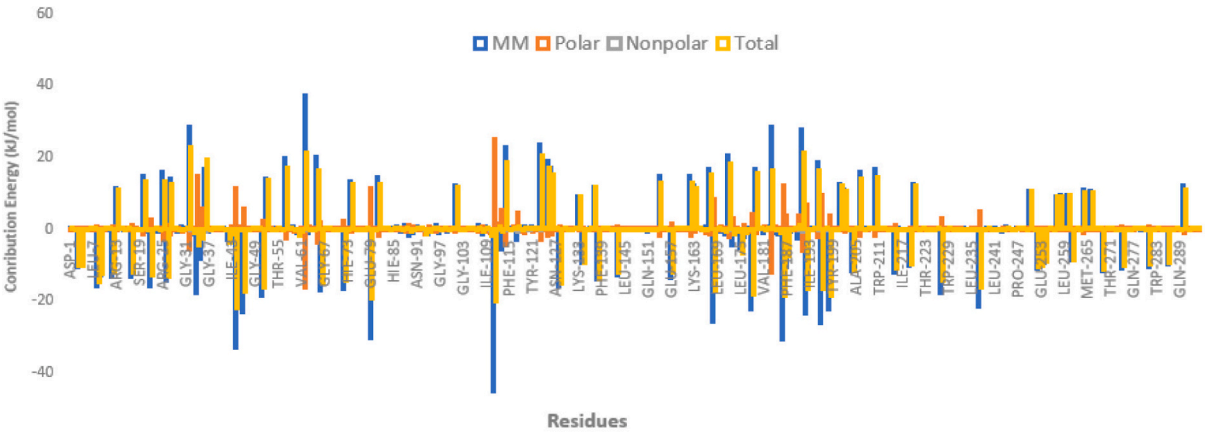

(a)

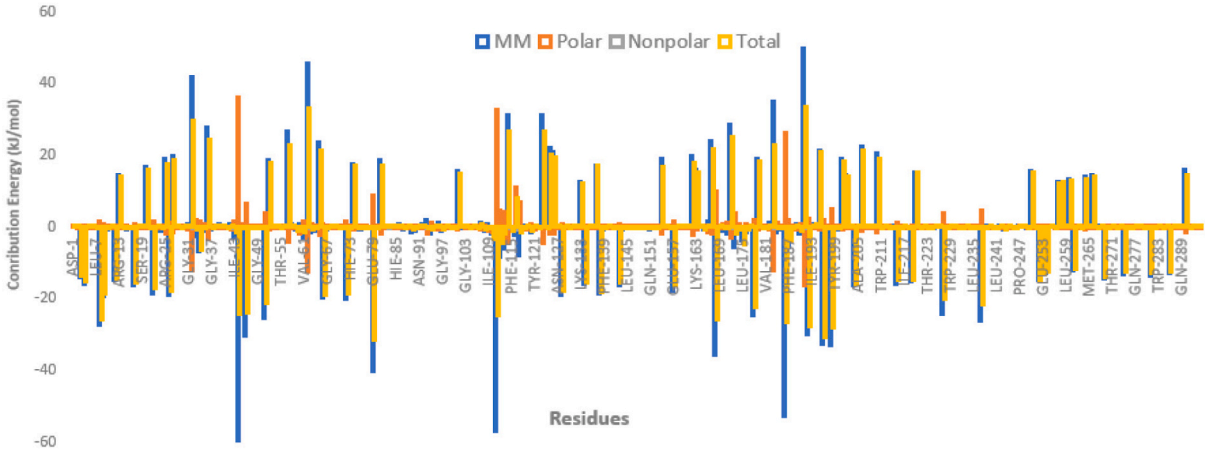

(b)

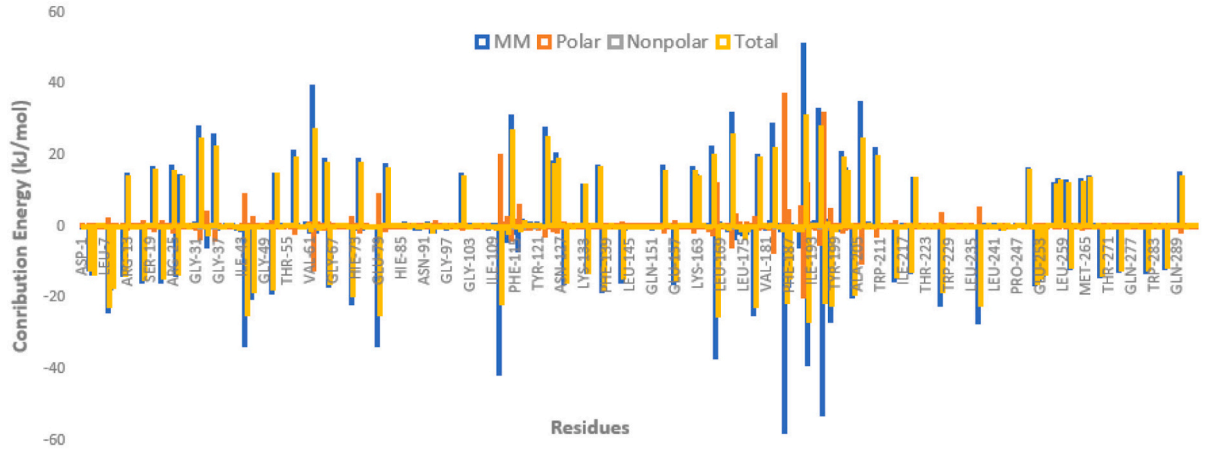

(c)

Fig. 8. Residue contribution energies **of** (a) *colig*-receptor (b) **comp1**-receptor (c) **comp2**-receptor (d) **comp3**-receptor.

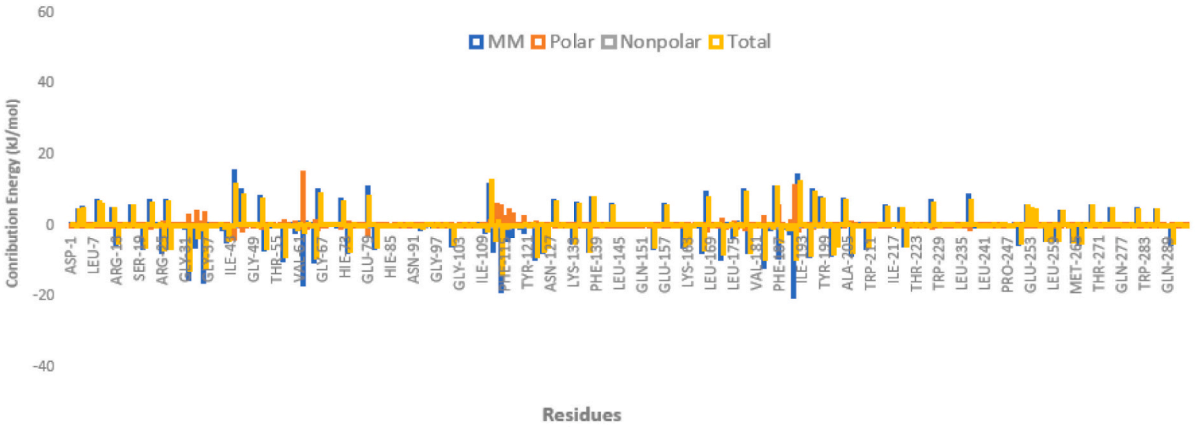

(d)

Fig. 8. (*continued*).

among residues like LEU838, VAL846, and PHE1045. For **comp3**, key contributions come from LEU838, VAL897, and PHE1045. Crucially, neither of these ligands benefits from the massive hydrophobic sum seen in *colig* or the powerful electrostatic spike from ASP1044 seen in **comp1**. This lack of a primary anchoring residue explains their weaker overall binding affinity and the greater conformational flexibility observed in their RMSD and RMSF profiles.

In conclusion, the per-residue decomposition elegantly clarifies the two successful binding strategies observed: high-affinity binding is achieved either through the cumulative effect of many strong hydrophobic interactions, as exemplified by *colig*, or through a powerful, single-point electrostatic anchor, as demonstrated by **comp1**.

3.7. Cytotoxicity results

The cytotoxic effects of **comp1**, **comp2**, and **comp3** were evaluated on HUVEC, HCT-116 and A549 cell lines using the MTT assay. All tested compounds showed IC_{50} values greater than 50 μM in all three cell lines, indicating low cytotoxicity toward both normal endothelial and cancer cells (Table 5). These results suggest that synthesized complexes do not exhibit a toxic profile at the tested concentrations and these findings are consistent with a VEGFR-2–centered anti-angiogenic mechanism rather than a direct tumoricidal effect.

The low cytotoxicity observed in HUVEC cells, together with the favorable binding characteristics revealed by docking and MD simulations, suggests that these complexes, particularly **comp1**, may serve as promising candidates for further development as VEGFR-2 targeting agents with minimal toxicity toward normal endothelial cells.

4. Conclusion

The integrated results from molecular docking, extensive molecular dynamics (MD) simulations, and quantum chemical analyses provide a comprehensive evaluation of the binding characteristics of the ligands in complex with the VEGFR-2 receptor.

Our findings consistently identify *colig* as the most potent and stable ligand across all metrics. It exhibited the most favorable binding free energy (ΔG_{bind} of −106.282 kJ/mol), a result driven by superior van der Waals interactions, as confirmed by both interaction energy calculations and per-residue decomposition analysis. This optimal steric fit is dynamically validated by its low and stable RMSD/RMSF profiles, which are anchored by a persistent network of hydrogen bonds throughout the simulation.

Among the synthesized palladium complexes, **comp1** emerges as the most promising candidate. Despite having a less favorable binding free energy (−74.742 kJ/mol) than *colig*, it demonstrated exceptional dynamic stability, with an RMSD profile as low and stable as *colig*'s. Our analyses conclusively show that this stability is not derived from hydrogen bonds but from a unique and powerful electrostatic anchor with the ASP1044 residue. This single interaction is strong enough to rigidify the entire complex, making **comp1** a highly effective, albeit mechanistically distinct, binder.

In contrast, **comp2** and **comp3** proved to be dynamically less stable. Their weaker binding free energies (ΔG_{bind} of −50.897 and − 58.741 kJ/mol, respectively) were mirrored by high and fluctuating RMSD and RMSF values. The analyses revealed that these ligands lack a single dominant anchoring interaction—neither the superior hydrophobic fit of *colig* nor the powerful electrostatic anchor of **comp1**—which results in greater conformational flexibility and weaker overall binding.

The quantum chemical analyses provided a deeper electronic rationale for these observations. We found that overall chemical reactivity (indicated by the energy gap, ΔE) did not correlate with binding affinity. However, a strong correlation was observed between the ligand's electron-donating capacity (HOMO energy) and its binding strength, underscoring the importance of charge-transfer character in the key non-covalent interactions.

In conclusion, this integrated computational study clarifies two distinct pathways to achieving stable VEGFR-2 inhibition: maximizing hydrophobic and van der Waals forces through shape complementarity (the *colig* strategy), or establishing a dominant electrostatic anchor point (the **comp1** strategy). Importantly, MTT assays revealed low cytotoxicity for all synthesized complexes (IC_{50} > 50 μM) on HUVEC cells, confirming their favorable safety profile. Considering its unique and potent binding mechanism, high dynamic stability, and low toxicity, **comp1** stands out as the most promising synthesized candidate for further development. VEGFR-2 inhibitors are being developed as potential drugs to block angiogenesis in cancer treatment. Future drug design efforts could focus on optimizing this structural framework,

Table 5
IC_{50} values obtained by MTT analysis of **comp1**, **comp2**, **comp3** and Cisplatin. Experiments were repeated at least 3 times.

Compounds	IC_{50} Values		
	HUVEC	HCT-116	A549
Comp1	>50	>50	>50
Comp2	>50	>50	>50
Comp3	>50	>50	>50
Cisplatin	3.85 ± 0.2	4.11 ± 0.7	11.2 ± 1.8

perhaps by combining the powerful electrostatic anchor of **comp1** with the superior hydrophobic features of *colig* to develop next-generation anticancer agents.

Availability of data and material

CCDC 2334591, 2334592 and 2334593 contain the supplementary crystallographic data for the compound reported in this article. These data can be obtained free of charge on application to CCDC, 12 Union Road, Cambridge CB2 1EZ, UK [Fax: +441,223 336,033, e-mail: deposit@ccdc.cam.ac.uk, https://www.ccdc.cam.ac.uk/structures/].

Authors contribution

BK and EAA performed methodology, synthesis and investigation, TK, OŞ, TBD and BÜ wrote and critically revised the manuscript. All authors read and approved the Final manuscript.

CRediT authorship contribution statement

Tuncay Karakurt: Writing – original draft, Supervision, Software. **Büşra Kaya:** Investigation, Data curation, Conceptualization. **Onur Şahin:** Writing – original draft, Software. **Elif Avcu Altıparmak:** Methodology, Data curation, Conceptualization. **Tülay Bal-Demirci:** Writing – review & editing, Supervision, Project administration. **Bahri Ülküseven:** Writing – review & editing, Supervision, Project administration.

Consent for publication

Not applicable.

Ethics approval and consent to participate

This work did not require ethical approval from a human subject or animal welfare committee.

Funding

This study was supported by Scientific Research Projects Coordination Unit of İstanbul University-Cerrahpaşa (Project number: FBA-2024-37346).

Declaration of competing interest

The authors declare that they have no known competing financial interests or personal relationships that could have appeared to influence the work reported in this paper.

Acknowledgement

The authors acknowledge to Scientific and Technological Research Application and Research Center, Sinop University, Turkey, for the use of the Bruker D8 QUEST diffractometer. The numerical calculations reported in this paper were fully/partially performed at TUBITAK ULAKBIM, High Performance and Grid Computing Center (TRUBA resources).

Appendix A. Supplementary data

Supplementary data to this article can be found online at https://doi.org/10.1016/j.inoche.2025.115860.

Data availability

Data will be made available on request.

References

[1] B. Rosenberg, L. van Camp, J.E. Trosko, V.H. Mansour, Platinum compounds: a new class of potent antitumour agents, Nature 222 (1969) 385–386. https://www.nature.com/articles/222385a0.
[2] O.D.H. Al-Mouqdady, A.S. Al-Janabi, M.R. Hatshan, S.A. Al-Jibori, A.S. Fiahan, C. Wagner, Synthesis, characterization, anti-bacterial and anticancer activities of palladium(II) mixed ligand complexes of 2-mercapto-5-methyl-1,3,4-thiadiazole (HmtzS) and phosphines, crystal structure of [Pd(mtzS)2(dppf)].H2O.EtOH, J. Mol. Struct. 1264 (2022) 133219, https://doi.org/10.1016/j.molstruc.2022.133219.
[3] B.B. Zmejkovski, N.Đ. Pantelić, G.N. Kaluđerović, Palladium(II) complexes: structure, development and cytotoxicity from cisplatin analogues to chelating ligands with N stereocenters, Inorg. Chim. Acta 534 (2022) 120797, https://doi.org/10.1016/j.ica.2022.120797.
[4] M.P. Dhaduk, R.A. Dabhi, B.S. Bhatt, V.D. Bhatt, M.N. Patel, Palladium(II)-quinoxaline based complexes: DNA/BSA binding, DFT, docking and anticancer activity, Mater. Today Proc. 65 (2022) 221–228, https://doi.org/10.1016/j.matpr.2022.06.119.
[5] E.Z. Jahromi, A. Divsalar, A.A. Saboury, S. Khaleghizadeh, H. Mansouri-Torshizi, I. Kostova, Palladium complexes: new candidates for anti-cancer drugs, J. Iran. Chem. Soc. 13 (2016) 967–989, https://doi.org/10.1007/s13738-015-0804-8.
[6] M. Vojtek, M.P.M. Marques, I.M.P.L.V.O. Ferreira, H. Mota-Filipe, C. Diniz, Anticancer activity of palladium-based complexes against triple-negative breast cancer, Drug Discov. Today 24 (4) (2019) 1044–1058, https://doi.org/10.1016/j.drudis.2019.02.012.
[7] A. Arafath, Thiosemicarbazone Schiff base ligands and their complexes with nickel, palladium and platinum show anticancer and antibacterial activities, J. Sulfur Chem. 45 (1) (2024) 138–171, https://doi.org/10.1080/17415993.2023.2255711.
[8] M. Jiang, W. Li, J. Liang, M. Pang, S. Li, G. Xu, M. Zhu, H. Liang, Z. Zhang, F. Yang, Developing a palladium(II) agent to overcome multidrug resistance and metastasis of liver tumor by targeted multiacting on tumor cell, inactivating cancer-associated fibroblast and activating immune response, J. Med. Chem. 67 (18) (2024) 16296–16310, https://doi.org/10.1021/acs.jmedchem.4c01175.
[9] W.O. Misigo, L.W. Njenga, R.A. Odhiambo, M. Meyer, L. Julius, N. Sibuyi, R. A. Lalancette, M.O. Onani, New thiosemicarbazones and their palladium(II) complexes: synthesis, spectroscopic characterization, X-ray structure and anticancer evaluation, Inorg. Chim. Acta 558 (2023) 121746, https://doi.org/10.1016/j.ica.2023.121746.
[10] W. Li, S. Li, Z. Zhang, G. Xu, X. Man, F. Yang, H. Liang, Developing a multitargeted anticancer palladium(II) agent based on the His-242 residue in the IIA subdomain of human serum albumin, J. Med. Chem. 66 (13) (2023) 8564–8579, https://doi.org/10.1021/acs.jmedchem.3c00248.
[11] M. Muralisankar, S.M. Basheer, J. Haribabu, N.S.P. Bhuvanesh, R. Karvembu, A. Sreekanth, An investigation on the DNA/protein binding, DNA cleavage and in vitro anticancer properties of SNO pincer type palladium(II) complexes with N-substituted isatin thiosemicarbazone ligands, Inorg. Chim. Acta 466 (2017) 61–70, https://doi.org/10.1016/j.ica.2017.05.044.
[12] A.E. Hassan, S.A.H. Albohy, A.S. Elzaref, A.S. Elfeky, E.M. El-Fakharany, A. K. Saleh, A.M. Mahmoud, W.E. Elgammal, Metal complexes with thiosemicarbazone derivative and isatine: a promising new class of materials for biomedical and environmental applications, J. Photochem. Photobiol. A Chem. 455 (2024) 115764, https://doi.org/10.1016/j.jphotochem.2024.115764.
[13] Z. Afrasiabi, E. Sinn, J. Chen, Y. Ma, A.L. Rheingold, L.N. Zakharov, N. Rath, S. Padhye, Appended 1,2-Zaphthoquinones as anticancer agents 1: synthesis, structural, spectral and antitumor activities of ortho-naphthaquinone thiosemicarbazone and its transition metal complexes, Inorg. Chim. Acta 357 (1) (2004) 271–278, https://doi.org/10.1016/S0020-1693(03)00484-5.
[14] S. Padhye, Z. Afrasiabi, E. Sinn, J. Fok, K. Mehta, N. Rath, Antitumor metallothiosemicarbazonates: structure and antitumor activity of palladium complex of phenanthrenequinone thiosemicarbazone, Inorg. Chem. 44 (5) (2005) 1154–1156, https://doi.org/10.1021/ic048214v.
[15] A.P. Rebolledo, M. Vieites, D. Gambino, O.E. Piro, E.E. Castellano, C.L. Zani, E. M. Souza-Fagundes, L.R. Teixeira, A.A. Batista, H. Beraldo, Palladium(II) complexes of 2-benzoylpyridine-derived thiosemicarbazones: spectral characterization, structural studies and cytotoxic activity, J. Inorg. Biochem. 99 (3) (2005) 698–706, https://doi.org/10.1016/j.jinorgbio.2004.11.022.
[16] S. Halder, S.-M. Peng, G.-H. Lee, T. Chatterjee, A. Mukherjee, S. Dutta, U. Sanyal, S. Bhattacharya, Synthesis, structure, spectroscopic properties and cytotoxic effect of some thiosemicarbazone complexes of palladium, New J. Chem. 32 (2008) 105–114, https://doi.org/10.1039/B707448D.
[17] A.Q. Ali, S.G. Teoh, N.E. Eltayeb, M.B. Khadeer Ahamed, A.M.S. Abdul Majid, A.A. A. Almutaleb, Synthesis, structure and in vitro anticancer, DNA binding and cleavage activity of palladium (II) complexes based on isatinthiosemicarbazone derivatives, Appl. Organomet. Chem. 31 (2017) e3813, https://doi.org/10.1002/aoc.3813.
[18] E. Ramachandran, P. Kalaivani, R. Prabhakaran, N.P. Rath, S. Brinda, P. Poornima, V.V. Padma, K. Natarajan, Synthesis, X-ray crystal structure, DNA binding, antioxidant and cytotoxicity studies of Ni(ii) and Pd(ii) thiosemicarbazone complexes, Metallomics 4 (2) (2012) 218–227, https://doi.org/10.1039/c1mt00143d.
[19] N. Gómez, D. Santos, R. Vázquez, L. Suescun, Á. Mombrú, M. Vermeulen, L. Finkielsztein, C. Shayo, A. Moglioni, D. Gambino, C. Davio, Synthesis, structural characterization, and pro-apoptotic activity of 1-indanone thiosemicarbazone platinum(II) and palladium(II) complexes: potential as antileukemic agents, ChemMedChem 6 (2011) 1485–1494, https://doi.org/10.1002/cmdc.201100060.

[20] W. Hernández, J. Paz, A. Vaisberg, E. Spodine, R. Richter, L. Beyer, Synthesis, characterization, and in vitro cytotoxic activities of benzaldehyde thiosemicarbazone derivatives and their palladium (II) and platinum (II) complexes against various human tumor cell lines, Bioinorg. Chem. Appl. 2008 (2009) 9, https://doi.org/10.1155/2008/690952. Article ID 690952.
[21] W. Hernández, J. Paz, F. Carrasco, A. Vaisberg, E. Spodine, J. Manzur, L. Hennig, J. Sieler, S. Blaurock, L. Beyer, Synthesis and characterization of new palladium(II) thiosemicarbazone complexes and their cytotoxic activity against various human tumor cell lines, Bioinorg. Chem. Appl. 2013 (2013) 12. Article ID 524701, https://doi.org/10.1155/2013/524701.
[22] F.H. Shah, Y.S. Nam, J.Y. Bang, I.S. Hwang, D.H. Kim, M. Ki, H.-W. Lee, Targeting vascular endothelial growth receptor-2 (VEGFR-2): structural biology, functional insights, and therapeutic resistance, Arch. Pharm. Res. 48 (2025) 404–425, https://doi.org/10.1007/s12272-025-01545-1.
[23] W.E. Elgammal, A.H. Halawa, I.H. Eissa, H. Elkady, A.M. Metwaly, S.M. Hassan, A. M. El-Agrody, Design, synthesis, and anticancer evaluation of N-sulfonylpiperidines as potential VEGFR-2 inhibitors, apoptotic inducers, Bioorg. Chem. 145 (2024) 107157, https://doi.org/10.1016/j.bioorg.2024.107157.
[24] I.H. Eissa, W.E. Elgammal, H.A. Mahdy, S. Zara, S. Carradori, D.Z. Husein, M. N. Alharthi, I.M. Ibrahim, E.B. Elkaeed, H. Elkady, A.M. Metwaly, Design, synthesis, and evaluation of novel thiadiazole derivatives as potent VEGFR-2 inhibitors: a comprehensive in vitro and in silico study, RSC Adv. 14 (2024) 35505–35519, https://doi.org/10.1039/D4RA04158E.
[25] H. Elkady, W.E. Elgammal, H.A. Mahdy, S. Zara, S. Carradori, D.Z. Husein, A. A. Alsfouk, I.M. Ibrahim, E.B. Elkaeed, A.M. Metwaly, I.H. Eissa, Anti-proliferative 2,3-dihydro-1,3,4-thiadiazoles targeting VEGFR-2: design, synthesis, in vitro, and in silico studies, Comput. Biol. Chem. 113 (2024) 108221, https://doi.org/10.1016/j.compbiolchem.2024.108221.
[26] W.E. Elgammal, H. Elkady, H.A. Mahdy, D.Z. Husein, A.A. Alsfouk, B.A. Alsfouk, I. M. Ibrahim, E.B. Elkaeed, A.M. Metwaly, I.H. Eissa, Rationale design and synthesis of new apoptotic thiadiazole derivatives targeting VEGFR-2: computational and in vitro studies, RSC Adv. 13 (2023) 35853–35876, https://doi.org/10.1039/D3RA07562A.
[27] H.A. Mahdy, H. Elkady, W.E. Elgammal, E.B. Elkaeed, A.A. Alsfouk, I.M. Ibrahim, D.Z. Husein, M.A. Elkady, A.M. Metwaly, I.H. Eissa, Design, synthesis, in vitro, and in silico studies of new thiadiazol derivatives as promising VEGFR-2 inhibitors and apoptosis inducers, J. Mol. Struct. 1316 (2024) 139019, https://doi.org/10.1016/j.molstruc.2024.139019.
[28] I.H. Eissa, H. Elkady, W.E. Elgammal, H.A. Mahdy, E.B. Elkaeed, A.A. Alsfouk, I. M. Ibrahim, D.Z. Husein, A.M. Metwaly, Integrated in silico and in vitro discovery of a new anticancer thiadiazole analog targeting VEGFR-2, J. Mol. Struct. 1312 (2024) 138641, https://doi.org/10.1016/j.molstruc.2024.138641.
[29] A. Ahmad, M.I. Nawaz, Molecular mechanism of VEGF and its role inpathological angiogenesis, J. Cell. Biochem. 123 (2022) 1938–1965, https://doi.org/10.1002/jcb.30344.
[30] P.A. Harris, A. Boloor, M. Cheung, R. Kumar, R.M. Crosby, R.G. Davis-Ward, et al., Discovery of 5-[[4-[(2, 3-dimethyl-2 H-indazol-6-yl) methylamino]-2-pyrimidinyl] amino]-2-methyl-benzenesulfonamide (Pazopanib), a novel and potent vascular endothelial growth factor receptor inhibitor, J. Med. Chem. 51 (15) (2008) 4632–4640, https://doi.org/10.1021/jm800566m.
[31] X. Wang, A.M. Bove, G. Simone, B. Ma, Molecular bases of VEGFR-2-mediated physiological function and pathological role, Front. Cell Dev. Biol. 8 (2020) 599281, https://doi.org/10.3389/fcell.2020.599281.
[32] A. Siddique, S. Shaheen, A. Iftikhar, A. Faisal, H.M. Rehman, M. Shah, A. Tahir, U. Rashid, Bicyclic 2-aminopyrimidine derivatives as potent VEGFR-2 inhibitors and apoptosis inducers: structure-guided design, synthesis, anticancer assessment, and in-silico exploration, Eur. J. Med. Chem. 293 (2025) 117726, https://doi.org/10.1016/j.ejmech.2025.117726.
[33] M. Aziz, R. Serya, D. Lasheen, et al., Discovery of potent VEGFR-2 inhibitors based on furopyrimidine and thienopyrimidne scaffolds as cancer targeting agents, Sci. Rep. 6 (2016) 24460, https://doi.org/10.1038/srep24460.
[34] E.B. Elkaeed, R.G. Yousef, M.M. Khalifa, A. Ibrahim, A.B.M. Mehany, I.M. M. Gobaara, B.A. Alsfouk, W.M. Eldehna, A.M. Metwaly, I.H. Eissa, et al., Discovery of new VEGFR-2 inhibitors: design, synthesis, anti-proliferative evaluation, docking, and MD simulation studies, Molecules 27 (19) (2022) 6203. https://www.mdpi.com/1420-3049/27/19/6203.
[35] Lv Yongcong, L. Mengyuan, T. Liu, L. Tong, T. Peng, L. Wei, J. Ding, H. Xie, W. Duan, Discovery of a new series of naphthamides as potent VEGFR-2 kinase inhibitors, ACS Med. Chem. Lett. 5 (5) (2014) 592–597. https://pubs.acs.org/doi/10.1021/ml5000417.
[36] M.M. Shirzad, N. Kulabaş, Ö. Erdoğan, Ö. Çevik, D. Dere, K. Yelekçi, Ö. Danış, İ. Küçükgüzel, Novel azole-urea hybrids as VEGFR-2 inhibitors: synthesis, in vitro antiproliferative evaluation and in silico studies, J. Mol. Struct. 1294 (2) (2023) 136448, https://doi.org/10.1016/j.molstruc.2023.136448.
[37] A. Chakraborty, S. Roy, M.P. Chakraborty, S.S. Roy, K. Purkait, T.S. Koley, R. Das, M. Acharya, A. Mukherjee, Cytotoxic ruthenium(II) complexes of pyrazolylbenzimidazole ligands that inhibit VEGFR2 phosphorylation, Inorg. Chem. 60 (23) (2021) 18379–18394, https://doi.org/10.1021/acs.inorgchem.1c02979.
[38] S. Aydinlik, A. Uvez, H.T. Kiyan, E. Gurel-Gurevin, V.T. Yilmaz, E. Ulukaya, E. Ilkay Armutak, Palladium (II) complex and thalidomide intercept angiogenic signaling via targeting FAK/Src and Erk/Akt/PLCγ dependent autophagy pathways in human umbilical vein endothelial cells, Microvasc. Res. 138 (2021) 104229, https://doi.org/10.1016/j.mvr.2021.104229.
[39] X.-Y. Qin, Y.-N. Wang, X.-P. Yang, J.-J. Liang, J.-L. Liu, Z.-H. Luo, Synthesis, characterization, and anticancer activity of two mixed ligand copper(ii) complexes by regulating the VEGF/VEGFR2 signaling pathway, Dalton Trans. 46 (2017) 16446–16454. https://pubs.rsc.org/en/content/articlelanding/2017/dt/c7dt03242k.
[40] S. Jayakumar, D. Mahendiran, T. Srinivasan, G. Mohanraj, A. Kalilur Rahiman, Theoretical investigation, biological evaluation and VEGFR2 kinase studies of metal(II) complexes derived from hydrotris(methimazolyl)borate, J. Photochem. Photobiol. B Biol. 155 (2016) 66–77, https://doi.org/10.1016/j.jphotobiol.2015.11.013.
[41] C. Yamazaki, The structure of isothiosemicarbazones, Can. J. Chem. 53 (1975) 610–615.
[42] B. Kaya, JOTCSA 9 (3) (2022) 867–878, https://doi.org/10.1016/j.molstruc.2017.08.079.
[43] F. Danışman Kalındemirtaş, B. Kaya, E. Sert, O. Şahin, S. Erdem Kuruca, Bahri Ülküseven, New oxovanadium(IV) complexes overcame drug resistance and increased in vitro cytotoxicity by an apoptotic pathway in breast cancer cells, Chem. Biol. Interact. 363 (2022) 109997, https://doi.org/10.1016/j.cbi.2022.109997.
[44] R.E. Malekshah, M. Salehi, M. Kubicki, A. Khaleghian, Crystal structure, molecular docking, and biological activity of the zinc complexes with 2-thenoyltrifluoroacetone and N-donor heterocyclic ligands, J. Mol. Struct. 1150 (2017) 155–165, https://doi.org/10.1016/j.molstruc.2017.08.079.
[45] T. Mosmann, Rapid colorimetric assay for cellular growth and survival: application to proliferation and cytotoxicity assays, J. Immunol. Methods 65 (1983) 55–63, https://doi.org/10.1016/0022-1759(83)90303-4.
[46] D. Özerkan, O. Ertik, B. Kaya, S.E. Kuruca, R. Yanardağ, B. Ülküseven, Novel palladium (II) complexes with tetradentate thiosemicarbazones. Synthesis, characterization, in vitro cytotoxicity and xanthine oxidase inhibition, Invest. New Drugs 37 (2019) 1187–1197, https://doi.org/10.1007/s10637-019-00751-1.
[47] R. Prabhakaran, K. Palaniappan, R. Huang, M. Sieger, W. Kaim, P. Viswanathamurthi, F. Dallemer, K. Natarajan, Can geometry control the coordination behaviour of 2-hydroxy-1-naphthaldehyde-N(4)-phenylthiosemicarbazone? A study towards its origin, Inorg. Chim. Acta 376 (1) (2011) 317–324, https://doi.org/10.1016/j.ica.2011.06.045.
[48] T. Bal, B. Ülküseven, Hydroxy and methoxy substituted N^1,N^4-diarylidene-S-methylthiosemicarbazone iron(III) and nickel(II) complexes, Trans. Met. Chem. 29 (2004) 880–884, https://doi.org/10.1007/s11243-004-2240-y.
[49] Tarlok S. Lobana, Activation of C–H bonds of thiosemicarbazones by transition metals: synthesis, structures and importance of cyclometallated compounds, RSC Adv. 5 (2015) 37231–37274, https://doi.org/10.1039/C5RA03333K.
[50] M.J. Abraham, T. Murtola, R. Schulz, S. Páll, J.C. Smith, B. Hess, E. Lindahl, GROMACS: high performance molecular simulations through multi-level parallelism from laptops to supercomputers, SoftwareX 1-2 (2015) 19–25, https://doi.org/10.1016/j.softx.2015.06.001.
[51] D.A. Case, H.M. Aktulga, K. Belfon, I.Y. Ben-Shalom, J.T. Berryman, S.R. Brozell, D. S. Cerutti, et al., "Amber 2023" (2023), University of California, San Francisco, 2023.
[52] R. Kumari, R. Kumar, A. Lynn, g_mmpbsa-a GROMACS tool for high-throughput MM-PBSA calculations, J. Chem. Inf. Model. 54 (2014) 1951–1962, https://doi.org/10.1021/ci500020m.
[53] E. Wang, H. Sun, J. Wang, Z. Wang, H. Liu, J.Z.H. Zhang, T. Hou, End-point binding free energy calculation with MM/PBSA and MM/GBSA: strategies and applications in drug design, Chem. Rev. 119 (16) (2018) 9478–9508, https://doi.org/10.1021/acs.chemrev.9b00055.
[54] S. Genheden, U. Ryde, The MM/PBSA and MM/GBSA methods to estimate ligand-binding affinities, Expert Opin. Drug Discovery 10 (5) (2015) 449–461, https://doi.org/10.1517/17460441.2015.1032936.
[55] N.A. Baker, Improving implicit solvent simulations: Poisson-Boltzmann or generalized born? Curr. Opin. Struct. Biol. 15 (2) (2005) 137–143, https://doi.org/10.1016/j.sbi.2005.02.001.
[56] N. Homeyer, N.H. Gohlke, Free energy calculations by the molecular mechanics Poisson-Boltzmann surface area method, Mol. Inf. 31 (2) (2012) 114–122, https://doi.org/10.1002/minf.201100135.